X-ray Spectroscopy of Galactic Hot Gas along the PKS 2155-304 Sight Line

Toshishige Hagihara[1], Yangsen Yao[2], Noriko Y. Yamasaki[1], Kazuhisa Mitsuda[1],
Q. Daniel Wang[3], Yoh Takei[1], Tomotaka Yoshino[1] * and Dan McCammon[4]

[1]*Institute of Space and Astronautical Science, Japan Aerospace Exploration Agency, 3-1-1, Yoshinodai, Chuo, Sagamihara, 252-5210*

hagihara@astro.isas.jaxa.jp, yamasaki@astro.isas.jaxa.jp

[2]*University of Colorado, CASA, 389 UCB, Boulder, CO 80309, USA*

[3]*Department of Astronomy, University of Massachusetts, Amherst, MA 01003, USA*

[4]*Department of Physics, University of Wisconsin, Madison, 1150 University Avenue, Madison, WI 53706, USA*

hagihara@astro.isas.jaxa.jp, yamasaki@astro.isas.jaxa.jp

Abstract

We present a detailed spectroscopic study of the hot gas in the Galactic halo toward the direction of a blazer PKS 2155-304 (z =0.117). The O VII and O VIII absorption lines are measured with the Low and High Energy Transmission Grating Spectrographs aboard *Chandra*, and the O VII, O VIII, and Ne IX emission lines produced in the adjacent field of the PKS 2155-304 direction are observed with the X-ray Imaging Spectrometer aboard *Suzaku*. Assuming vertically exponential distributions of the gas temperature and the density, we perform a combined analysis of the absorption and emission data. The gas temperature and density at the Galactic plane are determined to be $2.5(+0.6, -0.3) \times 10^6$ K and $1.4(+0.5, -0.4) \times 10^{-3}$ cm^{-3} and the scale heights of the gas temperature and density are $5.6(+7.4, -4.2)$ kpc and $2.3(+0.9, -0.8)$ kpc, respectively. These values are consistent with those obtained in the LMC X-3 direction.

Key words: Galaxy: disk - Galaxy: halo - X-rays: diffuse background - X-rays: ISM

1. Introduction

X-ray observations of edge-on spiral galaxies revealed the existence of hot gas at temperatures of $\sim 10^6$ K extending a few kpc beyond the disk (e.g. Wang et al. 2001; Wang et al. 2003; Strickland et al. 2004; Li et al. 2008; Yamasaki et al. 2009). The origin of energy and material in such a hot halo has not been clarified. Feedback from supernovae (SNe) as galactic wind or fountain and heated primordial gas are possible candidates (Norman & Ikeuchi 1989). In any cases, halo gas plays important roles in galactic evolution through chemical circulation and interaction between galaxies and the intergalactic medium.

The hot gaseous halo in and around the Milky-Way has been investigated for a long time. For instance, ROSAT All Sky Survey (RASS) quantitatively mapped the spatial distribution of the Soft X-ray Background emission (SXB; Snowden et al. 1997). The Cosmic X-ray Background (CXB) component extrapolated from the discrete hard X-ray sources could explain only about half of the SXB, leaving the soft X-ray emission below 1 keV being of a diffuse origin. With the high resolution X-ray microcalorimeter flying on a sounding rocket, McCammon et al. (2002) detected emission lines of hydrogen- and helium-like oxygen, neon, and iron ions from about 1 steradian of the sky, which suggests that the emitting gas is of a thermal

nature and at temperatures of T$\sim 10^6$ K. The existence of the hot gas in and around the Milky-Way is consistent with the *Chandra* observations of nearby edge-on spiral galaxies. However, because these emission data carry very little distance information, the properties of the global hot gas, like its density, temperature, and their distributions, are still poorly understood.

A combined analysis of high resolution absorption and emission data provides us with a powerful diagnostic of properties of the absorbing/emitting plasma. Absorption lines measure the column density of the absorbing material, which is an integration of the density of the absorbing ions along a sight line. In contrast, emission line intensity is sensitive to the emission measure, which is proportional to the density square of the emitting plasma. Thus, a combination of the emission and absorption data naturally yields the density and the size of the corresponding absorbing/emitting gas.

With significantly improved spectral resolution of current X-ray instruments, we are now able to observe the needed high resolution absorption and emission lines produced in the hot plasma. For instance, the X-ray absorption lines at $z = 0$, in particular the helium- and hydrogen-like O VII and O VIII lines, are detected in spectra of many galactic and extragalactic sources (e.g. Futamoto et al. 2004; Yao & Wang 2005; Williams et al. 2007). Recently, Fang et al. (2006) and Bregman & Lloyd-Davies (2007) find that the O VII absorption line can always be detected in an AGN spectrum as long as the spectrum is of

---

* Present Address is NEC corporation, Nisshin-cho 1-10, Fuchu, Tokyo 183- 8551

high signal-to-noise ratio. On the other hand, the X-ray Imaging Spectrometer (XIS) aboard *Suzaku* can also resolve emission lines produced in a diffuse emitting plasma at temperatures of T$\sim 10^6$ K. And indeed, the O VII and O VIII lines have been detected in nearly all directions (e.g., Smith et al. 2007; Shelton et al. 2007). Recently, a systematical study of emission lines of the hot gas in and around the Galaxy has been conducted by Yoshino et al. (2009), who report the O VII and O VIII lines in 14 blank sky observations with the XIS and conclude that the line-of-sight mean temperatures of the emitting gas has a narrow distribution around 2.3×10^6 K. Since the ion fractions of O VII and O VIII and their K-transition emissivities are very sensitive to gas temperature at $\sim 10^6$ K , a combined analysis of these emission and absorption lines will also constrain the gas temperature and its distribution without the complexity of relative chemical abundances of metal elements.

Although this combined analysis method has long been applied in the ultraviolet wavelength band (Shull & Slavin 1994), its application in the X-ray band just began. Complementing the high resolution absorption data observed with *Chandra* with the broadband emission data obtained with RASS, Yao & Wang (2007) firstly attempted to conduct the combined analysis in the X-ray band to infer the hot gas properties in our Galaxy. They also proposed a model for the Galactic disk assuming the temperature and density of the hot gas fading off exponentially along the vertical direction. They concluded that the O VII and O VIII absorption lines observed along the Mrk 421 sight line are consistent with the Galactic disk origin. Yao et al. 2009 further constrained this disk model by jointly analyzing the high resolution absorption data obtained with *Chandra* along the LMC X-3 sight line and emission data observed with *Suzaku* in the vicinity of the sight line. They estimated gas temperature and density at the Galactic plane and their scale heights as 3.6 (+0.8, −0.7) $\times 10^6$ K and 1.4 (+2.0, −1.0) $\times 10^{-3}$ cm^{-3} and 1.4 (+3.8, −1.2) kpc and 2.8 (+3.6, −1.8) kpc, respectively. These results are consistent with the early findings by Yao & Wang (2007), i.e., the SXB can be explained by a kpc-scale halo around our Galaxy.

In this paper, we present the second case study of the combined analysis of high resolution absorption and emission lines. The absorption lines are observed with *Chandra* along a blazer, PKS 2155–304 sight line and the emission lines are obtained with *Suzaku* observations of the vicinity of the sight line. In Section 2, we describe our observations and data reduction process. We perform our data analysis in Section 3 and discuss our results in Section 4.

2. Observations and Data Reduction

2.1. Chandra Observations and Data Reduction

Chandra observed PKS 2155–304 many times. There are two grating spectrographs (the low and high energy transmission grating spectrographs; LETG and HETG) and two sets of detectors (the advanced CCD imaging spectrometer; ACIS and the high resolution camera;
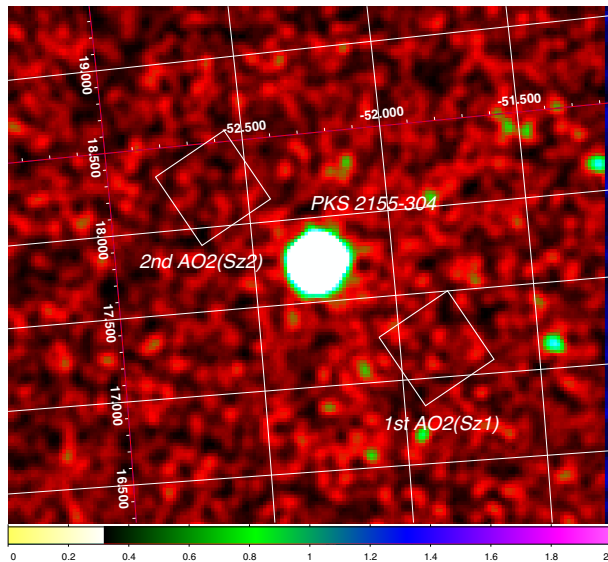
Fig. 1. RASS 0.1 - 2.4 keV band X-ray map in the vicinity of PKS 2155-304 (the bright source at the center) and the XIS field of view of the two presented observations.

HRC) aboard *Chandra* [1]. In this work, we used all observations available to the date of 2009 March, except for some observations made with non-standard configuration of ACIS (i.e., putting source outside the CCD-S3 chip) to avoid spectral resolution degradation. The data used in this work include 46 observations with an accumulated exposure time of 1.07 Ms.

We followed the standard scripts to calibrate the observations [2]. When extracting the grating spectra and calculating the instrumental response files, we used the same energy grid for all observations with different grating instruments and/or with different detectors for ease of the adding process described in the following. For those HETG observations, we only use the first order grating spectra of the medium energy grating (MEG) to utilize its large effective area at lower (< 1 keV) energy. For those observations taken with the HRC, we further followed the procedure presented in Yao et al. (2009) to extract the first order spectra of the LETG. We then added the first grating order spectra of all observations to obtain a single stacked spectrum and a corresponding instrumental response file.

### 2.2. Suzaku Observations and Data Reduction

We observed the emission of the hot diffuse gas toward two off-fields of the PKS 2155-304 sight line during the AO2 program (Table 1). To minimize confusion by stray lights from the PKS 2155-304 and to average out the possible spatial gradient of the diffuse emission intensity, the

---

[1]   please refer to the Chandra Observatory Guide for more information:
http://cxc.harvard.edu/proposer/POG/html/index.html

[2]   Please refer to the CIAO script for more information: http://cxc.harvard.edu/ciao/guides/

Table 1. *Suzaku* Observation Log

	Sz1	Sz2
(α, δ) in J2000 (degrees)	$(329.2236, -30.5193)$	$(330.1731, -29.9560)$
(ℓ, b) in Galactic coordinate (degrees)	$(17.1809, -51.8544)$	$(18.2418, -52.6081)$
Observation ID	503082010	503083010
Observation start times (UT)	18:32:39, 2008 Apr 29	08:31:41, 2008 May 2
Observation end times (UT)	08:30:08, 2008 May 2	17:30:19, 2008 May 4
Exposure time	90ks	87ks
Exposure after the data reduction	51.1ks	56.3ks
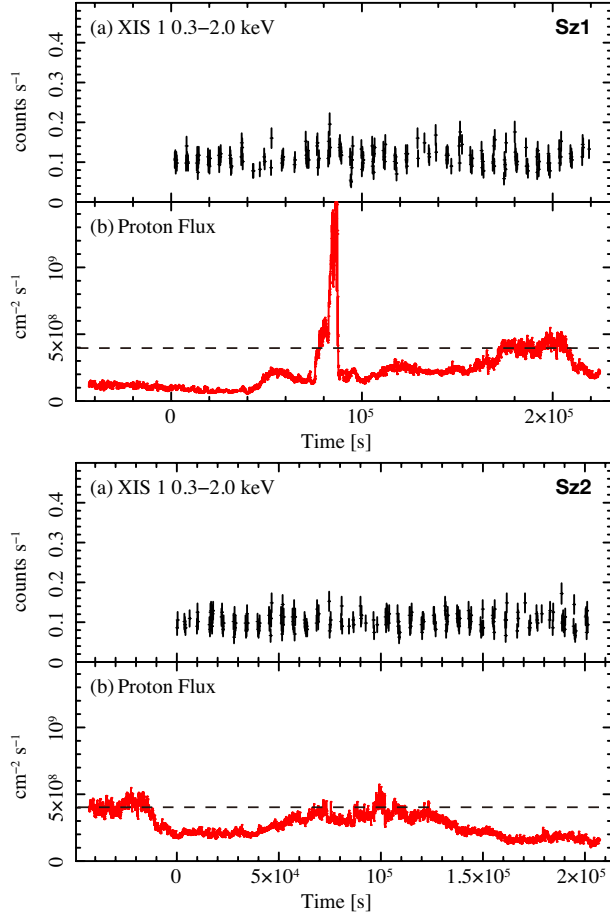
Fig. 2. (a) XIS light curve in 0.3-2.0 keV and (b) solar wind proton flux calculated using the data of ACE SWEPAM in Sz1 (top) and Sz2 (bottom) observation periods. The time is plotted from the beginning of each observation with *Suzaku*. The time bin of proton data are shifted 5000 seconds to correct for the travel time of the solar wind from the ACE satellite to the Earth. The dashed lines in the bottom panel indicate the threshold of the proton flux as 4×10^8 cm^{-2} s^{-1}.

two fields were chosen to be $30'$ away from the PKS 2155–304 and in nearly opposite directions (Fig. 1). With this configuration and the roll angle of the XIS field of view, we estimate that stray lights from PKS 2155-304 contribute no more than 10% to the observed X-ray emission in 0.3–1.0 keV energy range. Our observation pointings are away from the southern edge of Radio Loop I (Berkhuijsen et al. 1971). Thus we consider that there is no contamina-tion of the emission from the Loop I in our observations. This is supported by the observational results that there is no EUV enhancement in this direction (Sembach et al. 1997).

Our observations were taken with the CCD camera X-ray Imaging Spectrometer (XIS; Koyama et al. 2007) on board Suzaku (Mitsuda et al. 2007). The XIS was set to the normal clocking mode and the data format was either 3×3 or 5×5, and the spaced-raw charge injection (SCI) was applied to the data during the observations. We used processed data version 2.2.7.18 for the two observations. In this work, we only used the spectra obtained with XIS1. Compared to the other two front side-illuminated CCDs, XIS0 and XIS3, XIS1 is a backside-illuminated CCD chip and is of high sensitivity at photon energies below 1 keV. We found no point sources in the FOV, thus we used the full CCD field of view in further analysis to increase the photon counts because X-ray from the calibration sources do not affect the soft X-ray spectrum below 5 keV.

We adopted the standard data selection criteria to obtain the good time intervals (GTIs), i.e. excluding expo-sures when the line of sight of *Suzaku* is elevated above the Earth rim by less than $20°$ and exposures with the "cut-off rigidity" less than 8 GV. We checked the column density of the neutral oxygen in the Sun-lit atmosphere in the line of sight during the selected GTIs, and excluded the expo-sures when the column density is larger than 1.0×10^{15} cm^{-2} to avoid significant neutral oxygen emission from Earth's atmosphere (Smith et al. 2007). We created X-ray images in 0.4–1.0 keV energy range for the two observa-tions, and found no obvious discrete X-ray sources in the fields.

In the last step, we excluded those events severely con-taminated by the X-ray emission induced by the solar-wind charge exchange (SWCX) from geocorona (Fujimoto et al. 2007), meeting either of the following two crite-ria by Yoshino et al. (2009). The first one is the solar wind flux (Fig.2). We used the solar wind data obtained with the Solar Wind Electron Proton and Alpha Monitor (SWEPAM) aboard the *Advanced Composition Explorer* (*ACE*) and removed the time intervals when the proton flux in the solar wind exceeds 4×10^8 cm^{-2} s^{-1} (Masui et al. 2009). ACE is in L1 of the Solar-Earth system, 1.5×10^6 km away from the Earth and assuming average solar wind velocity as 300 km s^{-1}, we corrected traveling time of the solar wind from L1 to the Earth. The second criteria is the Earth-to-magnetopause (ETM) distance in

the line sight of Suzaku (Fujimoto et al. 2007), which is required to be $> 5R_E$. We found that about 20% and 5% of the exposure time of our 1st and 2nd observations meets the first criteria and no time meets the second criteria. Thus we exclude that 20% and 5% from 1st and 2nd observations and used the remaining time in further analysis. We also checked the light curve of XIS 1 in the energy range of 0.3 to 2.0 keV in the observation periods and found no evidence for variation (Fig. 2).

We constructed instrumental response files (rmfs) and effective area files (arf) by running the scripts *xisrmfgen* and *xissimarfgen* (Ishisaki et al. 2007). To take into account the diffuse stray light effects, we used a 20″ radius flat field as the input emission in calculating the arf. We also included in the arf file the degradation of low energy efficiency due to the contamination on the XIS optical blocking filter. The versions of calibration files used here were ae_xi1_quanteff_20080504.fits, ae_xi1_rmfparam_20080901.fits, ae_xi1_makepi_20080825.fits   and ae_xi1_contami_20071224.fits. We estimated the non-X-ray-background from the night Earth database using the method described in Tawa et al. (2008).

We grouped the spectra to have a minimum number of counts in each channel ≥ 50 and used energy range of 0.4–5.0 keV in our analysis. This range is broad enough for constraining the continuum and also covers the H- and He-like emission lines of N, O, Ne, Mg, and the L transition of Fe. The O VII, O VIII, and Ne IX lines are clearly visible in the spectra (Section 3.2).

3. Spectral Analysis and Results

We carried out our data analysis with the Xspec software package, adopting the solar abundances as given in Anders & Grevesse (1989). (Hereafter, use of *italic* type indicates Xspec models and their parameters.) Errors quoted throughout this paper are single parameter errors given at the 90 % confidence level, unless specified otherwise. Sections 3.1 and 3.2 give a discussion of our separate analyses of the absorption and emission data, while sections 3.3 and 3.4 give a discussion of the jointly–analyzed data under the uniform and exponential disk models.

3.1. Chandra X-ray Absorption Spectrum

We first measured the equivalent widths (EWs) of the absorption lines of the highly ionized oxygen ions. Becuase measurement of these narrow absorption lines is relevant only to the local continuum, we fit the final PKS 2155-304 spectrum between 0.55 and 0.7 keV as shown in figure 3 using a power-law model modified with absorption by the neutral ISM(*wabs*). The column density of neutral hydrogen was fixed to 1.47×10^{20} cm^{-2}, which is the value determined by the LAB Survey of Galactic HI in this direction (Kalberla et al. 2005). Three Gaussian functions were used to model the O VII K$_\alpha$, O VIII K$_\alpha$, and O VII K$_\beta$ absorption lines (model A1). The measured EWs were found to be consistent with those reported by Williams et al. 2007. The results are summarized in Table 2

Once the equivalent widths were determined, we applied an absorption line model, *absem*, to replace the *gaussian* functions in order to probe the properties of the absorbing gas. Assuming the temperature and density distributions of the hot plasma, the *absem* model, which is a revision of the *absline* model of Yao & Wang (2005), can be used to jointly fit the emission and absorption spectra. (See Yao & Wang (2007) and Yao et al. (2009) for a detailed description.) For a gas with a uniform density and a single temperature, the diagnostic procedure is summarized as follows: (1) A joint analysis of O VII K$_\alpha$ and O VII K$_\beta$ directly constrains the O VII column density and the Doppler dispersion velocity (v_b). With the constrained v_b, adding the O VIII K$_\alpha$ line in the analysis also yields the column density of O VIII (model A2). (2) Because the column density ratio of O VII and O VIII is sensitive to the gas temperature, a joint analysis of the O VII and O VIII lines will naturally constrain the gas temperature (model A3). (3) Assuming the solar abundance for oxygen and given the constrained gas temperature, the O VII (or O VIII) column density can be converted to the corresponding hot phase hydrogen column density (model A4). Table 3 gives the results of our fits. The constrained O VII column density, 5.9 (+1.2, −0.9) $\times 10^{15}$ cm^{-2} is comparable to typical values $\sim 10^{16}$ cm^{-2} obtained from AGN observations given in two systematic studies (Fang et al. (2006) and Bregman & Lloyd-Davies (2007)).
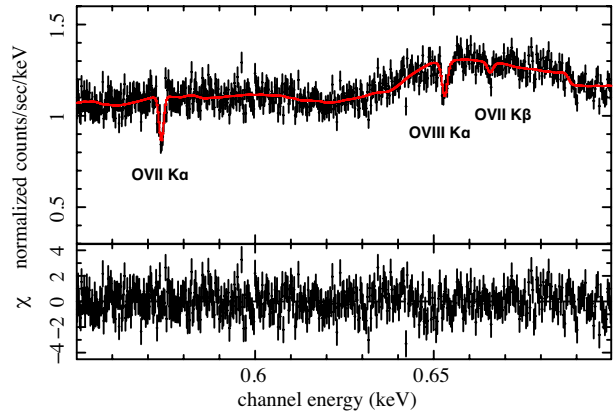
Fig. 3. Chandra spectrum of PKS 2155-304 between 0.55 and 0.7 keV. Fitted model is A4.

3.2. Suzaku X-ray Emission Spectra

The *Suzaku* data were modeled in order to constrain the emission measure and the temperature of the halo. For this purpose, we first modeled the SXB using a multiple component model, since the SXB emission is a superposition of such components. We detail this model below.

3.2.1. Foreground and Background Emission

We assumed that the SXB consists of four dominant components: (1) the Local Hot Bubble (LHB), (2) Solar Wind Charge eXchange in the heliosphere (SWCX), (3) a hot gaseous Galactic halo, (4) the cosmic X-ray background emission (CXB; mainly from unresolved extra-

Table 2. Spectral fitting results of absorption data with model A1

Model		O VII K_α	O VIII K_α	O VII K_β
A1	Centroid (eV)	$573.8^{+0.1}_{-0.2}$	$653.1^{+0.4}_{-0.4}$	$665.8^{+0.1}_{-0.4}$
	Sigma (eV)	$0.32^{+0.25}_{-0.32}$	$1.01^{+0.62}_{-0.54}$	$0.01^{+0.97}_{-0.01}$
	Equivalent Width (eV)	$0.354^{+0.075}_{-0.071}$	$0.377^{+0.116}_{-0.102}$	$0.119^{+0.058}_{-0.058}$

Model A1:$wabs(power\text{-}law+3\times Gaussian)$

Table 3. Spectral fitting results of absorption data with model A2-A4

Model	v_b (km s^{-1})	log [Column Density] (cm^{-2})			$\log T$ (K)	χ^2/dof
		$N_{\mathrm{O\,VII}}$	$N_{\mathrm{O\,VIII}}$	$N_{\mathrm{H_{Hot}}}$		
A2	294^{+149}_{-220}	$15.76^{+0.07}_{-0.08}$	$15.56^{+0.09}_{-0.12}$	$\cdots$	$\cdots$	489.82/474
A3	375^{+124}_{-158}	$15.77^{+0.08}_{-0.07}$	$\cdots$	$\cdots$	$6.27^{+0.02}_{-0.03}$	498.01/474
A4	290^{+152}_{-220}	$\cdots$	$\cdots$	$19.08^{+0.06}_{-0.07}$	$6.28^{+0.02}_{-0.02}$	489.84/474

Model A2,A3,A4:$wabs(power\text{-}law)\times absem\times absem\times absem$

galactic sources such as AGNs). Because the contribution from unresolved Galactic sources is expected to be negligible at high galactic latitudes ($|b| > 30°$), we did not consider such a contribution. The CXB spectrum is well described by a *power-law*.

In a study of 14 *Suzaku* blank sky observations, Yoshino et al. (2009) found that there are at least 2 LU (photons s^{-1}cm^{-2}str^{-1}) of OVII line emission even in those directions where the attenuation length for the line is less than 300 pc. This emission is considered to come from the SWCX and LHB, though these contributions are difficult to separate with the current CCD energy resolution. After Smith et al. (2007) and Henley et al. (2007), Yoshino et al. (2009) found that it can be well represented by a model consisting of unabsorbed, optically thin thermal emission from a collisionally-ionized plasma. The best-fit temperature of this model is $\log T = 6.06$. We therefore use a $\sim 10^6$ K plasma of 2 LU O VII surface brightness as the SWCX+LHB component. The uncertainty of this estimate is discussed in section 4.1.

Except for the SWCX+LHB component, the observed emission has been absorbed by the foreground ISM. In the following analysis, we also fix the neutral hydrogen column density to be 1.47×10^{20} cm^{-2} (Kalberla et al. 2005).

3.2.2. Spectral Fitting

To probe the halo gas properties, we used the following model to fit our spectra (model E1):
$wabs(power-law_{CXB} + vmekal_{halo}) + mekal_{LHB+SWCX}$,
with the photon index of the CXB fixed at 1.4 and with the normalization as a free parameter. The temperature and the corresponding emission measure (and thus the normalization) of the $mekal_{LHB+SWCX}$ component were set to be 1.2×10^6 K and 0.0043 pc cm^{-6}, respectively, correspondind to 2 LU of O VII K_α line emission. In the halo component, we fixed the abundance ratio of oxygen to hydrogen to the solar value, and allowed the abundances of nitrogen, neon, and iron vary.

This model fit the spectra from both pointings con-
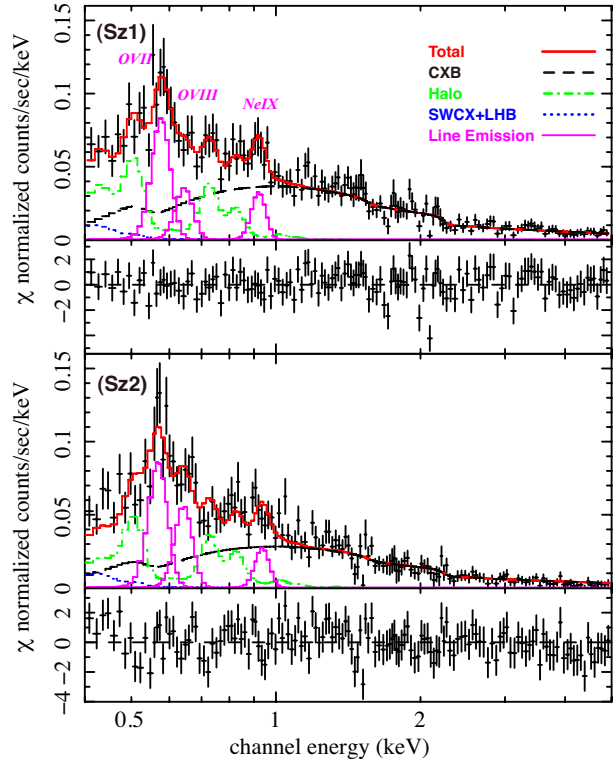
Fig. 4. Suzaku spectra between 0.4 and 5.0 keV of Sz1 (top) and Sz2 (bottom) are plotted. Fitted model is E2 ($wabs(power\text{-}law_{CXB} + vmekal_{halo}) + vmekal_{LHB+SWCX} + 3\times gaussians$). The O and Ne abundance of the $vmekal_{halo}$ (green, dash-dotted) and $vmekal_{LHB+SWCX}$ (blue, dotted) are set to be *zero* and three *gaussians* (magenta, solid) represent O VII K_α, (O VII K_β + O VIII K_α) and Ne IX K_α emission lines.

sistently, except for an apparently higher neon and iron abundance in Sz1 (Table 4) which would be caused by a lower temperature of the Sz1 halo component. It is important to clarify whether this is caused by statistical effects or by a true difference in plasma temperature. The sur-

Table 4. Spectral fitting results for emission data with the model E1

Model	Data	CXB Norm [a]	LHB+SWCX log T (K)	Norm[b]	halo log T (K)	Norm[b]	N/O	Ne/O	Fe/O	χ^2/dof
E1	Sz1	$8.40^{+0.38}_{-0.40}$	6.06(fixed)	4.3(fixed)	$6.26^{+0.06}_{-0.04}$	$3.3^{+1.0}_{-0.8}$	$6.0^{+2.5}_{-1.9}$	$6.5^{+3.7}_{-2.5}$	$7.4^{+13.8}_{-4.8}$	148.61/136
E1	Sz2	$6.45^{+0.36}_{-0.43}$	6.06(fixed)	4.3(fixed)	$6.35^{+0.03}_{-0.03}$	$3.2^{+0.5}_{-0.4}$	$4.7^{+2.0}_{-1.6}$	$2.4^{+1.2}_{-0.9}$	$1.0^{+0.8}_{-0.5}$	147.33/141
E1	Sz1+Sz2(Sz1)	$8.30^{+0.35}_{-0.39}$	6.06(fixed)	4.3(fixed)	$6.33^{+0.02}_{-0.02}$	$3.0^{+0.3}_{-0.3}$	$5.8^{+1.6}_{-1.3}$	$3.3^{+1.2}_{-0.9}$	$1.7^{+1.2}_{-0.7}$	306.82/282
	Sz1+Sz2(Sz2)	$6.50^{+0.36}_{-0.39}$	↑	↑	↑	↑	↑	↑	↑	
E1 [†]	Sz1+Sz2(Sz1)	$8.38^{+0.35}_{-0.36}$	6.06(fixed)	0.0(fixed)	$6.25^{+0.03}_{-0.02}$	$4.9^{+0.7}_{-0.6}$	$4.2^{+1.0}_{-0.8}$	$4.5^{+1.4}_{-1.2}$	$4.7^{+3.0}_{-1.6}$	313.48/282
	Sz1+Sz2(Sz2)	$6.59^{+0.34}_{-0.39}$	↑	↑	↑	↑	↑	↑	↑	
E1 [‡]	Sz1+Sz2(Sz1)	$8.25^{+0.38}_{-0.37}$	6.06(fixed)	7.5(fixed)	$6.37^{+0.03}_{-0.03}$	$2.3^{+0.3}_{-0.3}$	$6.9^{+2.4}_{-1.9}$	$3.2^{+1.3}_{-1.0}$	$1.5^{+0.9}_{-0.5}$	299.45/282
	Sz1+Sz2(Sz2)	$6.47^{+0.36}_{-0.38}$	↑	↑	↑	↑	↑	↑	↑	

↑ indicates linked parameters

Sz1+Sz2: simultaneous fitting of the data Sz1 and Sz2

Model E1: $wabs(power\text{-}law_{CXB} + vmekal_{halo}) + mekal_{LHB+SWCX}$

Emission measure of $mekal_{LHB+SWCX}$ is fixed to 0.0043cm^{-6} which corresponds to 2.0 LU of O VII K$_\alpha$ emission

[†] Emission measure of $mekal_{LHB+SWCX}$ is set to 0 as the lower limit

[‡] Emission measure of $mekal_{LHB+SWCX}$ is set to the upper limit which corresponds to 3.5 LU of O VII K$_\alpha$ emission

[a] in unit of photons cm^{-2} s^{-1}str^{-1} eV^{-1} @1keV

[b] Emission measure $10^{-3} \int n_e n_p dl$: in unit of cm^{-6} pc

Table 5. Surface brightness of O VII, O VIII and Ne IX

Model	Data	CXB Norm [a]	Norm[b]	halo N	Fe	O VII K$_\alpha$[c]	O VII K$_\beta$+ O VIII K$_\alpha$[c]	O VIII K$_\alpha$[c]	Ne IX K$_\alpha$[c]	χ^2/dof
E2	Sz1	$8.21^{+0.62}_{-0.27}$	$4.2^{+0.3}_{-0.8}$	6.0 (fixed)	7.4 (fixed)	$5.00^{+0.69}_{-0.80}$	$1.45^{+0.33}_{-0.51}$	$1.10^{+0.39}_{-0.56}$	$0.65^{+0.12}_{-0.26}$	136.39/132
E2	Sz2	$6.37^{+0.53}_{-0.26}$	$4.5^{+0.7}_{-0.6}$	4.7 (fixed)	1.0 (fixed)	$5.15^{+0.66}_{-0.86}$	$1.98^{+0.53}_{-0.37}$	$1.62^{+0.59}_{-0.42}$	$0.58^{+0.10}_{-0.29}$	150.59/137

model E2: $wabs(power\text{-}law_{CXB} + vmekal_{halo}) + vmekal_{LHB+SWCX} + 3\times gaussians$, where O and Ne abundances of two $vmekal$ are set to 0

[a] in unit of photons cm^{-2} s^{-1}str^{-1} eV^{-1} @1keV

[b] Emission Measure $10^{-3} \int n_e n_p dl$: in unit of cm^{-6} pc

[c] in unit of LU = photons s^{-1} cm^{-2} str^{-1}

face brightness of each line is a better indicator for this purpose.

We next evaluated the surface brightness of O VII and O VIII lines by modifying model E1 (this is model E2). We set the O and Ne abundance of the halo and LHB+SWCX to *zero* and used three *Gaussian* emission lines to represent O VII K$_\alpha$, (O VII K$_\beta$ + O VIII K$_\alpha$) and Ne IX K$_\alpha$ emission (Fig. 4). Since the XIS resolution is not high enough to enable us to distinguish the OVII K$_\beta$ (656 eV) and OVIII K$_\alpha$ (653 eV) lines, they were modeled as a single line. This model fitted both spectra with a χ^2/dof of 135.52/132 and 150.59/137 respectively. Assuming the ratio between O VII K$_\beta$, and O VII K$_\alpha (= \mu)$ intensities is 0.07 (see footnote 3) , we calculated the O VII, O VIII and Ne IX surface brightnesses as listed in Table 5. Intensities of these lines between the two fields are consistent to within the 90% confidence level, and we assume that the temperature dif-

ference is not essential. We plotted the O VII and O VIII surface brightness over the Yoshino et al. (2009) results (Fig. 5, with 1 σ error) and found that the O VII and O VIII surface brightness of the PKS 2155-304 direction matches the trend of the other 14 fields.

We next fitted both data sets simultaneously with model E1 by linking parameters of the halo component in both observations. The results are shown in Table 5. (Fig. 6). The emission measure for the model is 3.0 (+0.3, −0.3) ×10^{-3} cm^{-6} pc and the temperature is 2.1 (+0.1, −0.1) ×10^6 K. McCammon et al. (2002) reported the emission measure and temperature of the absorbed thermal component (=halo) as 3.7 ×10^{-3} cm^{-6} pc and 2.6 ×10^6 K which are comparable to our values.

3.3. Combined Analysis

Up to now, we have analyzed the absorption and emission data separately and confirmed that the models including the halo component fit both data with a temperature of 1.91(+0.09, −0.09) ×10^6 K for the absorption and 2.14 (+0.15, −0.14) ×10^6 K for the emission spectra.

---

3   μ is a slow function of the plasma temperature for thermal emission and here the value is 0.056. If the emission is due to SWCX, $\mu = 0.083$ (Kharchenko et al. 2003). We averaged these two values and used $\mu = 0.07$ here. See Yoshino et al. (2009) section 3.1 for details.
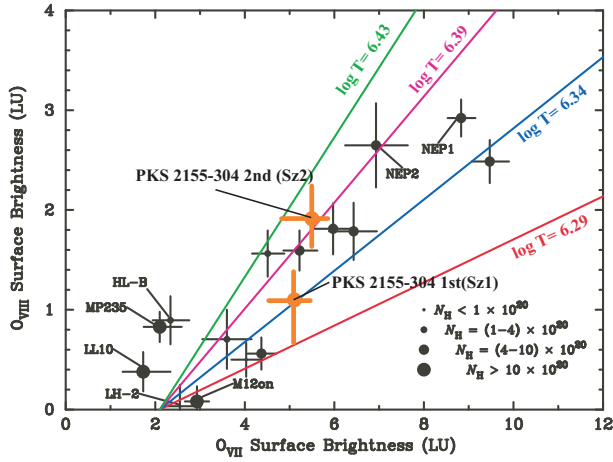
Fig. 5. Relation between O VII and O VIII surface brightnesses for the 14 (Yoshino et al. 2009)+2 (this work) sky fields observed with *Suzaku*. The horizontal and vertical bars of data points show the 1 σ errors of the estimate. The contribution of O VII K$_\beta$ emission is corrected for O VIII K$_\alpha$. The diagonal lines show the relation between O VII and O VIII, assuming an offset O VII emission of 2.1 LU and emission from a hot plasma of the temperature and the absorption column density are shown. The Galactic absorption column density of the observation fields are indicated by the maker size of the data points.
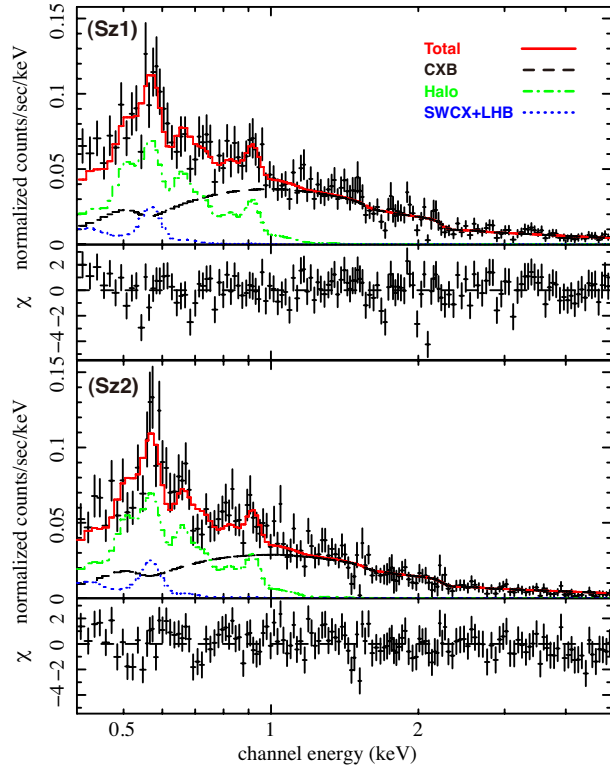
Fig. 6. Suzaku spectra between 0.4 and 2.0 keV. Sz1 (top) and Sz2 (bottom) observations are plotted. Fitted model is E1 ($wabs(power\text{-}law+vmekal\ _{halo})$ $+mekal_{LHB+SWCX}$) and parameters of the halo components are linked in both spectra.

Assuming that both plasmas are common and uniform, the plasma length and density can be calculated using

the emission measure and the column density. The length and density are found to be 4.0 (+1.9, −1.4) kpc and 7.7 (+2.3, −1.7) $\times 10^{-4}$ cm^{-3}, respectively. The errors of the calculated values are overestimated, since these errors are not independent. Moreover, important plasma parameters such as temperature and velocity dispersion were not considered in this simple calculation.

In this section, using the combined analysis, we will try to determine the physical conditions of the halo plasma, including the density, the temperature and their distribution.

3.3.1. Uniform Disk Model

The first step in our combined analysis was to try the simplest model: an isothermal plasma with uniform density extending up to h kpc above the disk (model C1).

To perform this combined analysis the emission measure and column density have to be linked with a common parameter. We chose the equivalent hydrogen column density ($N_{\mathrm{H_{Hot}}}$) and scale height (h) as the control parameters and calculated the emission measure. The relation of the density n, scale height h, column density $N_{\mathrm{H_{Hot}}}$ and galactic latitude b is described as $N_{\mathrm{H_{Hot}}} = nh/\sin b$. Thus we can use the A4 model for absorption data directly, and revise the E1 model to use the *vabmkl* instead of the *mekal* model. The *vabmkl* model, an extension of the *mekal* model, was constructed for the combined fit and used the column density and plasma length as the fit parameters. (see Yao et al. 2009 for a detailed model description). For the halo components of the emission spectra, we fixed the abundance ratio of oxygen to hydrogen to the solar value and allowed the abundances of nitrogen, neon, and iron to vary again. All parameters except for the normalization of the CXB components are linked over the two sets of emission data. We put lower and upper limits (70-440 km s^{-1}) to the velocity dispersion (v_b) which represent the 90 % error range of the values obtained by the absorption analysis.

The model C1 fits both data sets (χ^2/dof=802.78/754) and the results are given in Table 6. The column density and temperature are consistent with the A4 model (Table 3), while the temperature and abundance of Ne and Fe are not consistent with the E1 model (Table 4). This is because the temperature is mostly constrained by the absorption data and the lower temperature for the emission spectra preferred the higher abundance to describe the Ne and Fe lines. The plasma length is 4.2 (+1.5, −1.2) kpc and suggests that under the isothermal assumption the halo expands beyond the Galactic disk ($\sim$1 kpc).

3.3.2. Exponential Disk Model

Observations of edge-on galaxies(ex. Wang et al. 2003, Li et al. 2008, Yamasaki et al. 2009) have revealed that the intensities of X-ray emission from extended hot gas decreases exponentially as a function of height from the galactic plane. As a next step in our analysis, we employed another simple model to fit the data: an exponential distribution model (Yao et al. 2009). In this model, the density n and temperature T of the hot gas are distributed according to the following equation,

Table 6. Combined spectral fitting results with the uniform disk model

Model	Data	CXB Norm[a]	halo								χ^2/dof
			$\log N_{H_{Hot}}$ (cm^{-2})	h (kpc)	$\log T$ (K)	$v_b{}^\star$ (km s^{-1})	N/O	Ne/O	Fe/O	
C1	Emission:Sz1	$8.38^{+0.39}_{-0.38}$	$19.08^{+0.06}_{-0.07}$	$4.2^{+1.5}_{-1.2}$	$6.27^{+0.02}_{-0.02}$	$\cdots$	$4.9^{+1.4}_{-1.0}$	$5.2^{+1.4}_{-1.5}$	$5.0^{+1.6}_{-1.7}$	802.78/754
	Emission:Sz2	$6.57^{+0.39}_{-0.38}$	↑	↑	↑	$\cdots$	↑	↑	↑	
	Absorption	$\cdots$	↑	$\cdots$	↑	286^{+154}_{-206}	$\cdots$	$\cdots$	$\cdots$	

↑ indicates linked parameters
model C1: $wabs(power\text{-}law+vmekal)+mekal$ for the emission, $wabs(power)\times(absem)^3$ for the absorption
*Parameter range is limited to 70-440 km s^{-1}
[a]in unit of photons cm^{-2} s^{-1} str^{-1} eV^{-1} @1keV

$$n = n_0 e^{-Z/h_n \xi}, \quad T = T_0 e^{-Z/h_T \xi}, \quad \gamma = h_T/h_n \qquad (1)$$

where Z is the vertical distance from the Galactic plane, n_0 and T_0 are the density and temperature at the plane, and h_n and h_T are the scale heights of the density and temperature, respectively, and ξ is the filling factor, which is assumed to be 1 in this paper. Thus the equivalent hydrogen column density of the hot gas ($N_{H_{Hot}}$) is calculated as $N_{H_{Hot}} = \int_0^\infty n\,dl = \int_0^\infty n_0 \exp(-Z/h_n)dZ/\sin b = n_0 h_n/\sin b$.

The models $vabmkl$ and $absem$ can also be used in an exponential disk model using the additional parameter γ (see Yao et al. (2009) for detailed description). We therefore used the same model as used in the uniform model here (model C2). For fit parameters, for convenience we used the column density $N_{H_{Hot}}$ instead of n_0.

We jointly fitted the emission and absorption data using this exponential disk model. The parameters obtained are summarized in Table 7. We first fixed the velocity dispersion (v_b) at 290 km s^{-1}. We next examined the robustness of the temperature (T_0), column density ($N_{H_{HOT}}$), and scale height (h_n), as a function of γ, v_b, and the intensity of foreground SWCX intensity. We found that all parameters are consistent to within 90% statistical errors. When we fitted with v_b allowed to vary freely, the best-fit value of v_b became 54^{+19}_{-13} km s^{-1}. Though this is above the thermal velocity (~ 30 km s^{-1}), it is a smaller value than that obtained from the absorption spectrum which determined the ratio between the OVII K$_\alpha$ and K$_\beta$ lines. In the exponential disk model, low (3×10^5K $< T < 10^6$ K) temperature plasma can exist in the outer regions, which contribute only to the OVII absorption line. This might cause the smaller v_b value. The cooling time of such low temperature plasmas is very short, and the actual situation will not follow such a simple exponential model in this temperature range. We therefore fixed v_b at 290 km s^{-1}, as the best-fit value from the absorption analysis.

Confidence contours of h_n, T_0 and $N_{H_{Hot}}$ versus gamma are plotted in figure 7, over-laid on those of the LMC X-3 direction (Yao et al. 2009). We then obtained the scale height for the temperature gradient as $h_t = 5.6^{+7.4}_{-4.2}$ kpc and the gas density at the galactic plane as $n_0 = (1.4^{+0.5}_{-0.4}) \times 10^{-3}$ cm^{-3} (Figure 8). This values is typical for the mid-plane plasma density (Cox 2005). As the high temperature plasma close to the Galactic plane can emit Fe and Ne lines efficiently, the spectrum can be fitted without an abundance of heavy element higher than the
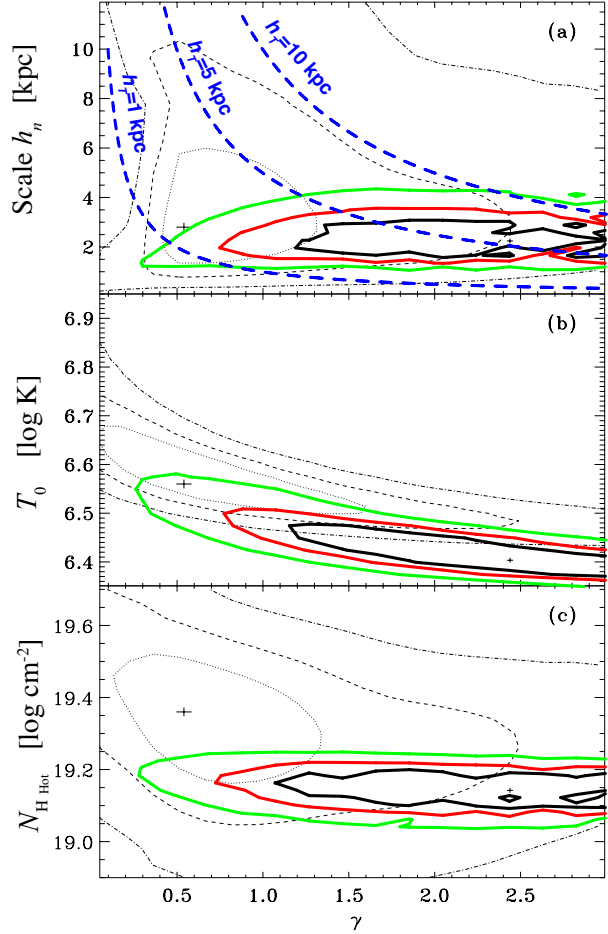
Fig. 7. 68%, 90%, and 99% confidence contours of h_n, T_0, and $N_{H_{Hot}}$ vs. γ, obtained from the combined fits to the X-ray absorption and emission data. Colored thick lines are for the PKS 2155-304 sight line, while the black thin lines are for the LMC X-3 sight lines (Yao et al. 2009). In the panel (a) the scale height of the temperature (h_T) is constant along the dashed lines.

solar value. The emission weighted temperature calculated with best fitted parameters using the intensity ratio of O VIII to O VII becomes $2.2(+0.1, -0.1) \times 10^6$ K.

Table 7. Combined spectral fitting results with the exponential disk model

Model	Data	CXB Norm^a	halo								χ^2/dof
			$\log N_{\mathrm{H_{Hot}}}$ (cm^{-2})	h_n (kpc)	$\log T_0$ (K)	$v_b{}^\star$ (km s^{-1})	γ	N/O	Ne/O	Fe/O	
C2	Emission:Sz1	$8.26^{+0.36}_{-0.37}$	$19.10^{+0.08}_{-0.07}$	$2.3^{+0.9}_{-0.8}$	$6.40^{+0.09}_{-0.05}$	$\cdots$	$2.44^{+1.11}_{-1.41}$	$5.8^{+1.6}_{-1.3}$	$3.1^{+1.6}_{-1.2}$	$1.5^{+1.0}_{-0.7}$	
	Emission:Sz2	$6.46^{+0.36}_{-0.36}$	↑	↑	↑	$\cdots$	↑	↑	↑	↑	
	Absorption	$\cdots$	↑	$\cdots$	↑	290 (fixed)	↑	$\cdots$	$\cdots$	$\cdots$	792.76/757
C2	Emission:Sz1	$8.20^{+0.39}_{-0.42}$	$19.13^{+0.07}_{-0.07}$	$2.2^{+0.5}_{-0.7}$	$6.48^{+0.04}_{-0.04}$	$\cdots$	1.0(fixed)	$6.1^{+1.8}_{-1.4}$	$2.4^{+0.9}_{-0.9}$	$1.0^{+0.6}_{-0.4}$	
	Emission:Sz2	$6.40^{+0.38}_{-0.41}$	↑	↑	↑	$\cdots$	↑	↑	↑	↑	
	Absorption	$\cdots$	↑	$\cdots$	↑	290 (fixed)	↑	$\cdots$	$\cdots$	$\cdots$	795.64/758
C2	Emission:Sz1	$8.25^{+0.33}_{-0.38}$	$19.10^{+0.07}_{-0.07}$	$2.4^{+0.9}_{-0.7}$	$6.38^{+0.02}_{-0.03}$	$\cdots$	3.5(fixed)	$5.6^{+1.1}_{-1.3}$	$3.3^{+1.2}_{-0.8}$	$1.7^{+0.3}_{-0.5}$	
	Emission:Sz2	$6.45^{+0.33}_{-0.37}$	↑	↑	↑	$\cdots$	↑	↑	↑	↑	
	Absorption	$\cdots$	↑	$\cdots$	↑	290 (fixed)	↑	$\cdots$	$\cdots$	$\cdots$	793.64/758
C2	Emission:Sz1	$8.17^{+0.37}_{-0.38}$	$19.41^{+0.19}_{-0.16}$	$5.1^{+3.9}_{-4.8}$	$6.51^{+0.16}_{-0.10}$	$\cdots$	$0.43^{+1.16}_{-0.23}$	$5.7^{+1.5}_{-1.3}$	$2.3^{+1.0}_{-1.0}$	$1.0^{+0.4}_{-0.5}$	
	Emission:Sz2	$6.37^{+0.37}_{-0.38}$	↑	↑	↑	$\cdots$	↑	↑	↑	↑	
	Absorption	$\cdots$	↑	$\cdots$	↑	70 (fixed)	↑	$\cdots$	$\cdots$	$\cdots$	789.75/757
C2	Emission:Sz1	$8.27^{+0.38}_{-0.33}$	$19.13^{+0.06}_{-0.07}$	$1.9^{+0.5}_{-0.3}$	$6.40^{+0.04}_{-0.05}$	$\cdots$	$2.84^{+1.34}_{-1.64}$	$5.8^{+1.7}_{-1.3}$	$3.2^{+1.1}_{-1.0}$	$1.6^{+0.5}_{-0.8}$	
	Emission:Sz2	$6.47^{+0.38}_{-0.32}$	↑	↑	↑	$\cdots$	↑	↑	↑	↑	
	Absorption	$\cdots$	↑	$\cdots$	↑	440 (fixed)	↑	$\cdots$	$\cdots$	$\cdots$	795.44/757
C2†	Emission:Sz1	$8.31^{+0.33}_{-0.41}$	$19.08^{+0.05}_{-0.07}$	$1.5^{+0.6}_{-0.5}$	$6.36^{+0.03}_{-0.07}$	$\cdots$	$3.39^{+2.40}_{-1.97}$	$4.9^{+1.1}_{-0.9}$	$3.2^{+0.7}_{-0.5}$	$2.0^{+0.9}_{-0.8}$	
	Emission:Sz2	$6.52^{+0.33}_{-0.41}$	↑	↑	↑	$\cdots$	↑	↑	↑	↑	
	Absorption	$\cdots$	↑	$\cdots$	↑	290(fixed)	↑	$\cdots$	$\cdots$	$\cdots$	803.71/757
C2‡	Emission:Sz1	$8.16^{+0.38}_{-0.39}$	$19.16^{+0.09}_{-0.08}$	$3.7^{+1.8}_{-1.1}$	$6.51^{+0.10}_{-0.07}$	$\cdots$	$1.47^{+0.52}_{-1.05}$	$7.2^{+2.4}_{-1.8}$	$2.2^{+1.3}_{-1.0}$	$0.9^{+0.6}_{-0.4}$	
	Emission:Sz2	$6.36^{+0.38}_{-0.38}$	↑	↑	↑	$\cdots$	↑	↑	↑	↑	
	Absorption	$\cdots$	↑	$\cdots$	↑	290(fixed)	↑	$\cdots$	$\cdots$	$\cdots$	783.37/757

↑ indicates linked parameters

model C2: $wabs(power\text{-}law+vabmkl)+mekal$ fot the emission, $wabs(power)\times(absem)^3$ for the absorption

†Emission measure of $mekal_{LHB+SWCX}$ is set to 0 as the lower limit.

‡Emission measure of $mekal_{LHB+SWCX}$ is set to upper limit which corresponds to 3.5 LU O VII K$_\alpha$ emission

^{a}in unit of photons cm^{-2} s^{-1} str^{-1} eV^{-1} @1keV

4. Discussion

4.1. Uncertainty due to of LHB and SWCX

Because our knowledge about the temporal and spatial variability of the SWCX and the LHB is limited, there are uncertainties due to the assumption of their intensity. These uncertainties could result in large uncertainties in our results.

To assess this uncertainty, we estimated the lower and upper values of the LHB and SWCX contributions and evaluated the parameters of the halo components again. The lower limit of the contribution is zero. As for the upper limit, we adopt 3.5 LU for the OVII emission, as obtained by the MBM 12 shadowing observation (Smith et al. 2007). As the heliospheric SWCX is caused by the collision between the Solar wind and the neutral ISM, the estimated emissivity has a peak around the ecliptic plane (Koutroumpa et al. 2007 , Lallement et al. 2004). MBM 12 is located at $(\lambda,\beta)=(47.4, 2.6)$ in ecliptic coordinates, while PKS2155-304 is at $(\lambda,\beta)=(321.2, -16.8)$. Thus we assume that the heliospheric SWCX contribution in the PKS 2155-304 direction could not be larger than that for MBM12.

The results using these lower and upper limits are shown in Table 4 and Table 7. Though the best fit values are slightly changed, they are consistent with the previous analysis.

4.2. Comparison with the Results for LMC X-3

We compared our results with those of the LMC X-3 direction, as is summarized in Table 8. The directions of the LMC X-3 and PKS 2155-304 are $(l,b) = (273.6, -32.1)$ and $(17.7, -52.2)$. The fact that we obtained similar values for the two directions indicates that the hot halo is common in the big picture and can be explained with the exponential model of the column density, scale height and temperature as $\sim 2 \times 10^{19}$ cm^{-2}, a few kpc and $\sim 2 \times 10^6$ K. As the distances to the targets are 50 kpc for LMC X-3 and 480 Mpc for PKS 2155-304, the consistency of the parameters of the exponential disk suggests that there is little contribution from beyond LMC X-3, or from a very extended halo of a 100 kpc scale.

4.3. Distribution of the O VII and O VIII Emitting/ Absorbing Gas and Its Origin

We calculated the distribution of O VII and O VIII ions and their emissivities assuming the best fit parameters at $\gamma = 2.44$ and at $\gamma = 1.0$ and 3.5 (Fig. 9).

We then estimated the total radiative energy loss from the thick disk distributed exponentially. Assuming solar
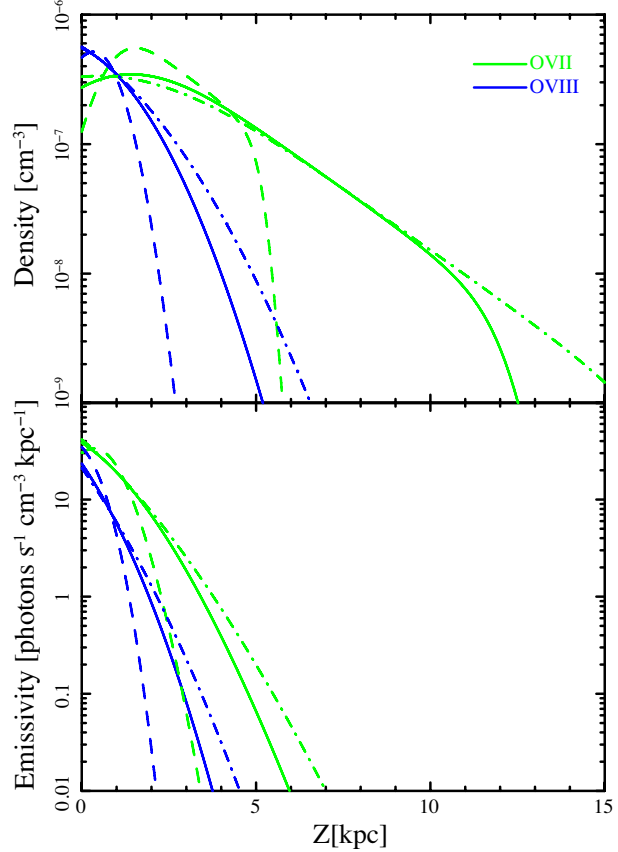
Table 8. Disk model parameters for two sight lines

Direction	log $N_{\mathrm{H_{Hot}}}$ (cm^{-2})	h_n (kpc)	$logT_0$ (K)	γ	Ne	Fe
PKS 2155-304	$19.10^{+0.08}_{-0.07}$	$2.3^{+0.9}_{-0.8}$	$6.40^{+0.09}_{-0.05}$	$2.44^{+1.11}_{-1.41}$	$3.1^{+1.6}_{-1.2}$	$1.5^{+1.0}_{-0.7}$
LMC X-3†	$19.36^{+0.22}_{-0.21}$	$2.8^{+3.6}_{-1.8}$	$6.56^{+0.11}_{-0.10}$	$0.5^{+1.2}_{-0.4}$	$1.7^{+0.6}_{-0.4}$	$0.9^{+0.2}_{-0.2}$

† from Yao et al. 2009
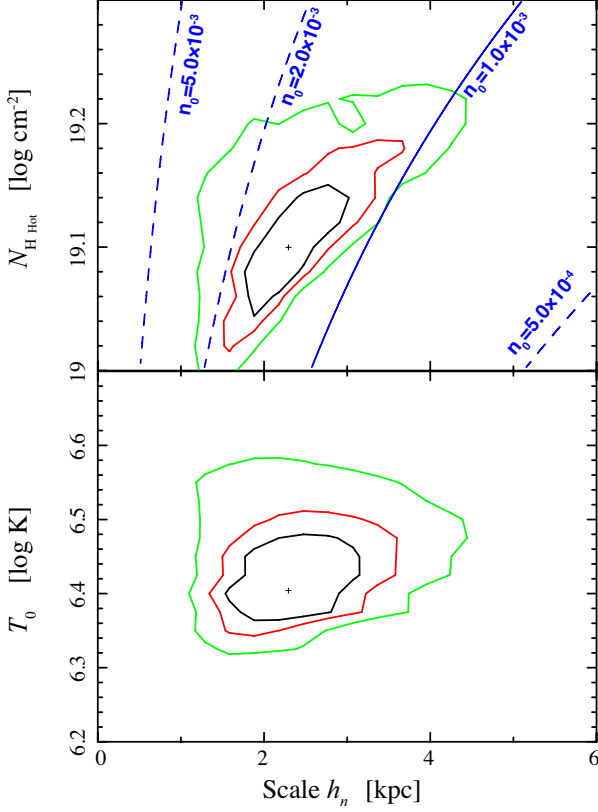
Fig. 8. 68%, 90%, and 99% confidence contours of T_0 and $N_{\mathrm{H_{Hot}}}$ vs. scale height h_n obtained in the joint fit to the X-ray absorption and emission data. In the upper panel the density at the plane n_0 is constant along the solid and dashed lines.

Fig. 9. The density of O VII and O VIII ion(top) and the emissivity of O VII and O VIII lines (bottom) as a function of the height from the galactic plane under the best fit parameter of γ=2.44 (solid line), γ=1.0 (dashed line) and γ=3.5 (dash-dotted line).

abundances, best fit parameters and ionization fraction and emissivity as taken from SPEX[4], we obtained the energy loss rate as a function of the distance from the Galactic plane Z (Fig. 10). We then integrated the energy loss rate until the temperature of the exponential disk become lower than $10^{5.5}$ K. Because our results are based on X-ray observations, it is difficult to detect plasma of T $< 10^{5.5}$ K. We obtained a total radiative energy loss rate of 7.2×10^{36} erg s^{-1} kpc^{-2} in 0.001–40 keV and 1.8×10^{35} erg s^{-1} kpc^{-2} in 0.3–8.0 keV. These values are consistent with the X-ray luminosity of other spiral galaxies (Strickland et al. 2004).

We next compared the energy loss rate with the energy input rate from SNe. According to Ferrière (1998), the SN rate near the sun is 19 Myr^{-1} kpc^{-2} for type II SNe and 2.6 Myr^{-1} kpc^{-2} for type Ia SNe, respectively. Assuming each SN explosion releases 1 $\times 10^{51}$ ergs, the total input energy is then 7 $\times 10^{38}$ ergs s^{-1} kpc^{-2}. If 1 % of the SN explosion energy is input to the hot halo, the total energy loss can be compensated.

4.4. Consistency with O VI Absorbing Gas

It is not clear that our model is consistent beyond ~ 5 kpc where the temperature of the gas is below $\sim 10^{6.0}$ K and O VI ion becomes dominant.

Williams et al. (2007) found two local O VI absorption lines in the *FUSE* PKS 2155-304 spectrum and reported column densities of $1.10\pm0.1 \times 10^{14}$ and $8.7\pm0.4 \times 10^{13}$ cm^{-2}. Our exponential disk model expects OVI column

---

^{4} http://www.sron.nl/index.php?option=com_content &task=view&id=125&Itemid=279
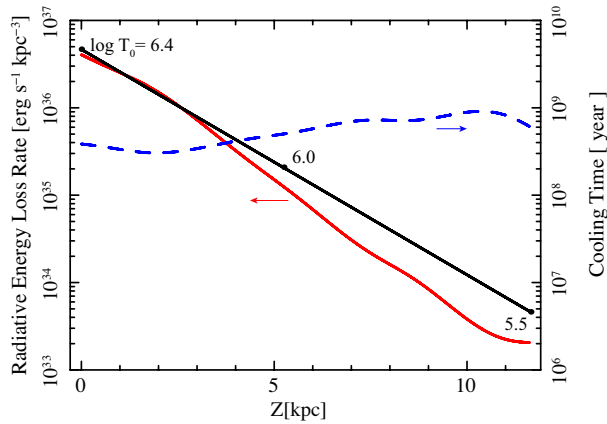
Fig. 10. Radiative energy loss rate (red, solid) and cooling time (blue, dashed) as a function of the distance from the Galactic plane. The temperature is indicated by the solid black line. The emissivity is calculated from the *mekal* model, using a script made by Sutherland. (http://proteus.pha.jhu.edu/~dks/Code/ Coolcurve_create/index.html)

densities of 3.8×10^{13}, 1.4×10^{14}, and 2.1×10^{13} cm^{-2} with the best fit parameters when γ=2.44, 1.0, and 3.5 respectively.

Howevera plasma emitting O VI lines cools very rapidly and it would be difficult to maintain such plasma existing high above the Galactic plane. Radiative cooling is accelerated by the density fluctuations. Thus OVI absorbing gas can be a patchy or blob-like condensation. To discuss this problem, energy and matter flow models are needed, which is beyond the focus of this paper.

5. Summary

We have analyzed high resolution X-ray absorption/emission data observed by *Chandra* and *Suzaku* to determine the physical state of the global hot gas along the PKS 2155-304 direction.

1. Suzaku clearly detected O VII K$_\alpha$, O VIII K$_\alpha$ and O VII K$_\beta$ lines. The surface brightnesses of O VII and O VIII in this direction can be understood in the same scheme as obtained by other 14 observations (Yoshino et al. 2009).
2. By the absorption analysis, column density is measured as 3.9 (+0.6,−0.6) cm^{-3} pc and temperature is measured as 1.91 (+0.09,−0.09) $\times 10^6$ K. By the emission analysis, emission measure is measured as 3.0 (+0.3,−0.3) $\times 10^{-3}$ cm^{-6} pc and temperature is measured as 2.14 (+0.15,−0.14) $\times 10^6$ K.
3. Combined analysis using the exponential disk model gives a good fit with χ^2/dof of 789.65/756 to both emission and absorption spectra. The gas temperature and density at the Galactic plane are determined to be $2.5(+0.6,−0.3) \times 10^6$ K and $1.4(+0.5,−0.4) \times 10^{-3}$ cm^{-3} and the scale heights of the gas temperature and density 5.6(+7.4,−4.2) kpc and 2.3(+0.9,−0.8) kpc, respectively.

4. The results obtained by the combined analysis are consistent with those for the LMC X-3 direction. This suggest that the global hot gas surrounding our Galaxy has common structure.

References

Anders, E., & Grevesse, N. 1989, Geochim. Cosmo chim. Acta, 53, 197

Berkhuijsen, E. M., Haslam, C. G. T., & Salter, C. J. 1971, A&A, 14, 252

Bregman, J. N., & Lloyd-Davies, E. J. 2007, ApJ, 669, 990

Cox, D. P. 2005, ARA&A, 43, 337

Fang, T., McKee, C.F., Canizares, C.R., Wolfire, M. 2006, ApJ, 644, 174

Ferrière, K. 1998, ApJ, 497, 759

Fujimoto, R., et al. 2007, PASJ, 59, S133

Futamoto, K., Mitsuda, K., Takei, Y., Fujimoto, R., & Yamasaki, N. Y. 2004, ApJ, 605, 793

Henley, D. B., Shelton, R. L., & Kuntz, K. D. 2007, ApJ, 661, 304

Ishisaki, Y., et al. 2007, PASJ, 59, 113

Kalberla, P. M. W., Burton, W. B., Hartmann, D., Arnal, E. M., Bajaja, E., Morras, R., P&oumlppel, W. G. L. 2005, A&A, 440, 775

Kharchenko, V., Rigazio, M., Dalgarno, A., & Krasnopolsky, V. A. 2003, ApJL, 585, L73

Koutroumpa, D., Acero, F., Lallement, R., Ballet, J., & Kharchenko, V. 2007, A&A, 475, 901

Koyama, K., et al. 2007, PASJ, 59, 23

Lallement, R., Raymond, J.C., Vallerga, J., Lemoine, M., Dalaudier, F., & Vertaux, J.L. 2004, A&A, 426, 875

Li, J.-T., Li, Z., Wang, Q. D., Irwin, J. A., & Rossa, J. 2008, MNRAS, 390, 59

Masui, K., Mitsuda, K., Yamasaki, N. Y., Takei, Y., Kimura, S., Yoshino, T., & McCammon, D. 2009, PASJ, 61, 115

McCammon, D., et al.2002, ApJ, 576, 188

Mitsuda, K., et al. 2007, PASJ, 59, 1

Norman, C. A., & Ikeuchi, S. 1989, ApJ, 345, 372

Sembach, K.R., Savage, B.D.m Tripp, T.D. 1997, ApJ, 480, 216

Shelton, R. L., Shallmen, S. M., & Jenkins, E. B. 2007, ApJ, 659, 365

Shull, J. M., & Slavin, J. D. 1994, ApJ, 427, 784

Smith, R. K., et al.2007, PASJ, 59, S141

Snowden, S. L., Egger, R., Freyberg, M. J., McCammon, D., Plucinsky, P.P., Sanders, W.T., Schmitt, J.H.M.M., Trümper, J., & Voges, W. 1997, ApJ, 485, 125

Strickland, D. K., Heckman, T. M., Colbert, E. J. M., Hoopes, C. G., & Weaver, K. A. 2004, ApJS, 151, 193

Sutherland, R. S., & Dopita, M. A. 1993, ApJS, 88, 253

Tawa, N. et al, 2008, PASJ, 60, S22

Williams, R. J., Mathur, S., Nicastro, F., & Elvis, M. 2007, ApJ, 665, 247

Wang, Q.D., Immler, S., Walterbos, R., Lauroesch, J. T, Breitschwerdt, D. 2001, ApJL, 555, 99

Wang, Q.D., Chaves, T., Irwin, J.D. 2003, ApJ, 598, 969

Yamasaki, N. Y., Sato, K., Mitsuishi, I., & Ohashi, T. 2009, PASJ, 61, 291

Yao, Y., & Wang, Q. D., 2005, ApJ, 624, 751

Yao, Y., & Wang, Q. D., 2007, ApJ, 658, 1088

Yao, Y., Wang, Q. D., Hagihara, T., Mitsuda, K., McCammon, D., & Yamasaki, N. Y. 2009, ApJ, 690, 143

Yoshino, T., et al. 2009, PASJ, 61, 805